

10. L. Lisiecki, M. Raymo, *Paleoceanography* **20**, 10.1029/2004PA001071 (2005).
11. M. Raymo, K. Nisancioglu, *Paleoceanography* **18**, 10.1029/2002PA000791 (2003).
12. K. Nisancioglu, thesis, Massachusetts Institute of Technology (2004).
13. P. Clark, R. Alley, D. Pollard, *Science* **286**, 1104 (1999).
14. E. Ziperman, H. Gildor, *Paleoceanography* **18**, 10.1029/2001PA000627 (2003).
15. D. Paillard, *Nature* **391**, 378 (1998).
16. P. Huybers, C. Wunsch, *Nature* **434**, 491 (2005).
17. A. Berger, X. Li, M. Loutre, *Quat. Sci. Rev.* **18**, 1 (1999).
18. R. DeConto, D. Pollard, *Palaeogeogr. Palaeoclimatol. Palaeoecol.* **198**, 39 (2003).
19. A. Berger, M. F. Loutre, *Earth Planet. Sci. Lett.* **111**, 369 (1992).
20. Daily average surface temperatures are estimated by using the network of 8892 World Meteorological Organization (WMO) stations above 30°N for the years 1994 to 1999. All stations that have greater than 80% data coverage are used. Data gaps are filled by linear interpolation. Stations are standardized to 1 km of elevation assuming a lapse rate of 6.5°C/km, were binned according to 1° or 10° latitude bands (as indicated in the text), and are then averaged together. Lastly, each of the six consecutive seasonal cycles are averaged together, yielding average annual cycles as a function of latitude.
21. C. Wunsch, *J. Clim.* **18**, 4374 (2005).
22. W. Paterson, *Physics of Glaciers* (Pergamon Press, Oxford, ed. 3, 1994).
23. R. Braithwaite, Y. Zhang, *J. Glaciol.* **152**, 7 (2000).
24. The use of a constant value for τ illustrates the concept of summer energy. A more detailed description would take into account that τ is expected to be spatially and temporally variable, depending on factors such as elevation, albedo, clouds, heat transport, and greenhouse gas concentrations. Note, however, that results are not sensitive to plausible choices of τ and that values less than 325 W/m² yield broadly consistent summer energies (fig. S1). Summer energy values at 65°N are given in table S1.
25. The relationship between insolation intensity and insolation energy is more precisely illustrated by noting that $I \propto 1/r^2$, where I is insolation intensity and r is the distance from the Earth to the Sun. Conservation of angular momentum (or, equivalently, Kepler's second law) dictates that $dt \propto r^2 d\lambda$, where dt is an infinitesimal change in time and $d\lambda$ the corresponding change in solar longitude. The energy received by the Earth is then $J = I dt \propto d\lambda$. In contrast with I , the J between any two solar longitudes is independent of r and, thus, independent of the precession of the equinoxes.
26. Are past changes in summer energy sufficient to cause the waxing and waning of ice sheets? Although a full answer requires a realistic model of Pleistocene climate, some indication is provided by modern glacial changes: A 2.4 W/m² global average increase in radiative forcing caused by greenhouse gases (34) has apparently led to a general decrease in glacial mass (35), suggesting that glaciers are sensitive to relatively small changes in the radiation budget.
27. C. Wunsch, *Clim. Dyn.* **20**, 353 (2003).
28. Materials and Methods are available as supporting material on Science Online.
29. Amplitude cross correlation was computed by pairing local maxima in insolation with the nearest (in time) maximum in the rate of change of ice volume. Before identifying maxima, both the $\delta^{18}\text{O}$ record and the summer energy were smoothed by using an 11-ky tapered window. There are 34 local maxima in summer energy at 65°N between 2 and 1 My ago and another 34 between 1 My ago and the present. Squared cross correlations of 0.4 and higher have P values of less than 0.01. Spectral and coherence analysis is performed by using Thomson's multitaper method (36).
30. J. C. Zachos, N. J. Shackleton, J. S. Revenaugh, H. Pälike, B. P. Flower, *Science* **292**, 274 (2001).
31. Similar with the early Pleistocene, late Pleistocene ice volume change has significant variability concentrated at the obliquity band, which is in phase and coherent with summer energy ($P = 0.01$). That the obliquity component of summer energy varies symmetrically between the hemispheres helps explain the symmetry of glacial variations between the hemispheres. Also, the increase in summer energy near 420 ky ago, absent in measures of summer insolation forcing relying on intensity, helps explain the corresponding glacial termination.
32. M. E. Raymo, *Paleoceanography* **12**, 577 (1997).
33. M. Raymo, *Annu. Rev. Earth Planet. Sci.* **22**, 353 (1994).
34. J. Houghton et al., Eds., *Climate Change 2001: The Scientific Basis. Contribution of Working Group I to the Third Assessment Report of the Intergovernmental Panel on Climate Change* (Cambridge Univ. Press, New York, 2001).
35. J. Oerlemans, *Science* **308**, 675 (2005); published online 3 March 2005 (10.1126/science.1107046).
36. D. Percival, A. Walden, *Spectral Analysis for Physical Applications* (Cambridge Univ. Press, Cambridge, 1993).
37. This paper benefited from discussion with E. Boyle, B. Curry, M. Raymo, P. Stone, E. Ziperman, and C. Wunsch. J. Levine provided valuable assistance in calculating the insolation. The NSF paleoclimate program supported this work under grant no. ATM-0455470.

Supporting Online Material

www.sciencemag.org/cgi/content/full/1125249/DC1

SOM Text

Figs. S1 to S3

References

23 January 2006; accepted 9 June 2006

Published online 22 June 2006;

10.1126/science.1125249

Include this information when citing this paper.

A Thick Cloud of Neptune Trojans and Their Colors

Scott S. Sheppard^{1*} and Chadwick A. Trujillo²

The dynamical and physical properties of asteroids offer one of the few constraints on the formation, evolution, and migration of the giant planets. Trojan asteroids share a planet's semimajor axis but lead or follow it by about 60° near the two triangular Lagrangian points of gravitational equilibrium. Here we report the discovery of a high-inclination Neptune Trojan, 2005 TN₅₃. This discovery demonstrates that the Neptune Trojan population occupies a thick disk, which is indicative of "freeze-in" capture instead of in situ or collisional formation. The Neptune Trojans appear to have a population that is several times larger than the Jupiter Trojans. Our color measurements show that Neptune Trojans have statistically indistinguishable slightly red colors, which suggests that they had a common formation and evolutionary history and are distinct from the classical Kuiper Belt objects.

The Neptune Trojans are only the fourth observed stable reservoir of small bodies in our solar system; the others are the Kuiper Belt, main asteroid belt, and jovian Trojans. The Trojan reservoirs of the giant planets lie between the rocky main belt asteroids and the volatile-rich Kuiper Belt. The effects of nebular gas drag (1), collisions (2), planetary

migration (3, 4), overlapping resonances (5, 6), and the mass growth of the planets (7, 8) all potentially influence the formation and evolution of the Neptune Trojans. The number of Jupiter Trojans is comparable to the main asteroid belt (9). One Neptune Trojan was discovered serendipitously in 2001 (10). Our ongoing dedicated Trojan survey has found three additional Neptune Trojans (Table 1).

Stable minor planets in the triangular Lagrangian Trojan regions, called the leading L4 and trailing L5 points, are said to be in a 1:1 resonance with the planet because each completes one orbit about the Sun with the period

of the parent planet. The Neptune Trojans are distinctly different from other known Neptune resonance populations found in the Kuiper Belt. Kuiper Belt resonances such as the 3:2 (which Pluto occupies) and 2:1 may owe their existence to sweeping resonance capture of the migrating planets (11). The Neptune Trojans, however, would be lost because of migration and are not captured during this process (3, 4, 10).

Numerical dynamical stability simulations have shown that Neptune may retain up to 50% of its original Trojan population over the age of the solar system after any marked planetary migration (4, 12). These simulations also demonstrate that Saturn and Uranus are not expected to have any substantial primordial Trojan populations. Recent numerical simulations of small bodies temporarily passing through the giant planet region, such as Centaurs, have shown that Neptune cannot currently efficiently capture Trojans even for short periods of time (4, 13). Thus, capture or formation of the Trojans at the Lagrangian regions likely occurred during or just after the planet formation epoch, when conditions in the solar system were vastly different from those now. We numerically integrated (14) several orbits similar to each of the known Neptune Trojans and found that the majority of test particles near each known Neptune Trojan were stable over the age of the solar system.

Various mechanisms have been proposed that dissipated asteroid orbital energy to perma-

¹Department of Terrestrial Magnetism, Carnegie Institution of Washington, 5241 Broad Branch Road NW, Washington, DC 20015, USA. ²Gemini Observatory, 670 North A'ohoku Place, Hilo, HI 96720, USA.

*To whom correspondence should be addressed. E-mail: sheppard@dtm.ciw.edu

nently capture bodies in the Lagrangian regions of the planets. Neptune’s formation was probably quite different from Jupiter’s (15), and thus gas drag (1) or rapid mass growth of the planet (2, 7), as suggested for Jupiter Trojan capture, was probably not effective near Neptune. This suggests that the formation and possible capture of Neptune’s Trojans was likely independent of the planet formation process. One possible mechanism is some type of “freeze-in” capture (6). This may occur if the orbits of the giant planets become excited and perturb many of the small bodies throughout the solar system. Once the orbits of the planets stabilize, any chance objects in the Lagrangian Trojan regions become stable and thus are trapped. A second mechanism proposed is collisional interactions within the Lagrangian region (2, 16), and a third possible mechanism is in situ accretion of the Neptune Trojans from a subdisk of debris formed from postmigration collisions (2). The two col-

Table 1. Trojan orbital elements and sizes. Orbital data shown for the known Neptune Trojans are the semimajor axis (*a*), inclination (*i*), and eccentricity (*e*). Also included are the median Jupiter Trojan data. All four known Neptune Trojans have been observed during at least two oppositions, including the Neptune Trojans discovered in 2005 from recovery observations in June 2006 using GMOS on the Gemini North 8.2-m telescope. The orbital data are from the Minor Planet Center (supporting online text). The radii (*r*) of the objects were calculated assuming an albedo of 0.05 (0.1) using the equation $r = [2.25 \times 10^{16} R^2 \Delta^2 / p_R \phi(0)]^{1/2} 10^{0.2(m_\odot - m_R)}$ where *R* is the heliocentric distance in AU, Δ is the geocentric distance in AU, m_\odot is the apparent red magnitude of the sun (−27.1), p_R is the red geometric albedo, m_R is the apparent red magnitude of the Trojan, and $\phi(0) = 1$ is the phase function at opposition. Our Neptune Trojan discovery survey used the Magellan-Baade 6.5-m telescope with the 0.2 square degree wide-field of view Inamori Magellan Areal Camera and Spectrograph (IMACS) for imaging. Survey data were obtained on the nights of UT 16 and 17 October 2004 and 6, 7, and 8 October 2005. Conditions over the different nights varied, but all were photometric, although wind and humidity limited our efficiency. We covered about 12 square degrees of the sky within about 1 hour of the Neptune L4 point in right ascension and within 1.5° of the ecliptic and Neptune’s orbit. The limiting magnitude of the images varied between about an R color band of 23.5 magnitudes in the poorest fields to near 25th magnitude in the best fields, with the average being between 24 and 24.5 magnitudes. We used a wide filter covering the typical V and R color bands for discovery.

Name	<i>a</i> (AU)	<i>i</i> (deg)	<i>e</i>	<i>r</i> (km)
2001 QR ₃₂₂	30.14	1.3	0.03	70 (50)
2004 UP ₁₀	30.08	1.4	0.03	50 (35)
2005 TN ₅₃	30.05	25.1	0.07	40 (30)
2005 TO ₇₄	30.05	5.3	0.06	50 (35)
Median Jup	~5.2	10.9	0.07	

lisional theories above predict low inclination Trojans, whereas freeze-in allows for high-inclination bodies.

Through our survey using the Magellan-Baade 6.5-m telescope, we have discovered one high-inclination (2005 TN₅₃; inclination *i* ~ 25 degrees) and two low-inclination (2004 UP₁₀ and 2005 TO₇₄; *i* < 5°) Trojans (Table 1). Because we have surveyed only in the low-latitude Neptune L4 region (within 1.5° of Neptune’s orbit and the ecliptic), we have been heavily biased toward finding low-inclination Trojans. We can correct for this bias by determining the probability of detecting high-inclination Trojans in our low-inclination fields. A high-inclination Trojan on a nearly circular orbit like 2005 TN₅₃ would only spend about 2% of its orbit within the 1.5° of ecliptic latitude that our survey covered. Thus, for every high-inclination Trojan discovered by our survey, we should expect tens of high-inclination Trojans (i.e., 50⁺⁷⁵_{−35}) outside this latitude range, assuming Poisson statistics. The low-inclination Trojans 2004 UP₁₀ (*i* ~ 1.4°) and 2005 TO₇₄ (*i* ~ 5°), respectively, spend about 50% and 10% of their orbits within our survey latitudes. Thus, the ratio of high- to low-inclination L4 Trojans is 50⁺⁷⁵_{−35}:12⁺¹⁰_{−7}, or about 4:1. Statistically, there may be at least as many, although most likely more, high-inclination Trojans as there are low-inclination Trojans. Our discovery of 2005 TN₅₃ indicates that the Neptune Trojan population occupies a thick disk, like the Jupiter Trojans. The collisional and in situ accretion Neptune Trojan formation models predict few, if any, high-inclination Trojans. Unless there has been recent excitation in the Neptune L4 region, freeze-in capture (6) or

some variation on it (17) appears to be the most likely capture process.

We further explored the physical properties of the Neptune Trojans by obtaining optical colors of each Trojan (Table 2). We found that the four known Neptune Trojans have indistinguishable optical colors, which are consistent with a common formation and evolution history for all. This is unlike the Kuiper Belt objects (KBOs), which show a large color diversity from gray to some of the reddest objects in the solar system (18). We found that the Neptune Trojans have optical colors a little redder than the gray KBOs (Fig. 1). The Neptune Trojans do not appear to have the extreme red colors shown by objects in the low-inclination (“cold”), high-perihelion classical Kuiper Belt (19, 20).

To determine whether the Neptune Trojans are drawn from the same distribution of colors as are other small-body populations, we performed some statistical tests. First, we note that about 30% of KBOs have colors similar to those of the Neptune Trojans (21). From this information, we find that there is less than a (0.3)⁴ ~ 1% chance of observing the Neptune Trojan colors we found if they are drawn from the same color distribution as the KBOs. We further performed a Monte Carlo Kolmogorov-Smirnov (K-S) test on the colors (Table 2). We first determined the maximum cumulative distance (D-statistic) of the four Neptune Trojan colors when ranking them versus each population individually. A Monte Carlo simulation was used to estimate the significance of the D-statistic because of our small data set, for which common analytic approximations on the significance fail when the two sample populations are not of equal size. We randomly chose

Table 2. Optical photometry. The mean colors of individual Neptune Trojans and some dynamical classes with the K-S test confidence of difference probabilities (K-S Diff) from Neptune Trojans are shown: Neptune Troj, Neptune Trojans; Jupiter Troj, Jupiter Trojans; KBOs, Kuiper Belt objects; cold KBOs, classical KBOs with *i* < 10° and KBOs with perihelion > 40 AU; Centaur blue, the blue lobe of the bimodal centaur distribution; Centaur red, the red lobe of the bimodal Centaur distribution; and Irr sats, Irregular satellites of the giant planets. Uncertainties listed for each dynamical class are the standard deviation showing the broadness of the color distribution. The standard deviation of the mean colors are much smaller, around 0.02 magnitudes. Color references are in the text.

Name	<i>m_R</i> (mag)	B-V (mag)	V-R (mag)	R-I (mag)	B-I (mag)
2001 QR ₃₂₂	22.50 ± 0.01	0.80 ± 0.03	0.46 ± 0.02	0.36 ± 0.03	1.62 ± 0.04
2004 UP ₁₀	23.28 ± 0.03	0.74 ± 0.05	0.42 ± 0.04	0.46 ± 0.05	1.63 ± 0.06
2005 TN ₅₃	23.73 ± 0.04	0.82 ± 0.08	0.47 ± 0.07	0.47 ± 0.09	1.75 ± 0.10
2005 TO ₇₄	23.21 ± 0.03	0.85 ± 0.06	0.49 ± 0.05	0.42 ± 0.06	1.76 ± 0.07
	K-S Diff				
Neptune Troj	0%	0.80 ± 0.05	0.46 ± 0.03	0.43 ± 0.05	1.69 ± 0.08
Jupiter Troj	45%	0.74 ± 0.05	0.45 ± 0.03	0.43 ± 0.03	1.63 ± 0.09
KBOs	99.2%	0.90 ± 0.15	0.57 ± 0.12	0.55 ± 0.13	2.08 ± 0.38
Cold KBOs	99.99%	0.98 ± 0.14	0.64 ± 0.10	0.57 ± 0.07	2.20 ± 0.29
Centaur blue	98%	0.92 ± 0.21	0.59 ± 0.15	0.58 ± 0.12	2.08 ± 0.47
Centaur red	15%	0.72 ± 0.05	0.45 ± 0.04	0.49 ± 0.07	1.66 ± 0.14
Comets	99.99%	1.11 ± 0.08	0.72 ± 0.05	0.67 ± 0.08	2.50 ± 0.20
Irr sats	95%	0.79 ± 0.05	0.49 ± 0.05	0.49 ± 0.12	1.78 ± 0.14
	55%	0.78 ± 0.11	0.47 ± 0.09	0.39 ± 0.12	1.63 ± 0.20

four colors 100,000 times from each non-Neptune Trojan population color distribution and determined the D-statistic each time in the same manner as we did using the four Neptune Trojans. The confidence limits in Table 2 represent the percentage of times the randomly drawn colors' D-statistic was lower than the actual Neptune Trojan colors' D-statistic for each population.

To date, the known Neptune Trojan population is too scant to formally reject them as being from the same color distribution as the KBOs with only a 99.2% confidence. However, we find the Neptune Trojan colors are different from the extremely red classical low-inclination and distant perihelion KBOs at the 99.99% confidence level. We also find they are incompatible with the red lobe of the Centaur bimodal color distribution at the 99.99% confidence level (Fig. 1). The Neptune Trojan colors are most consistent with the blue lobe of the possible bimodal Centaur color distribution (18). Further, the Neptune Trojans are also consistent with the color distributions of the Jupiter Trojans (22), irregular satellites (23), and possibly the comets (24).

These colors are consistent with a similar origin for the Neptune Trojans, the Jupiter Trojans, irregular satellites, and dynamically excited gray Kuiper Belt population. These populations may have been subsequently dispersed, transported, and trapped in their current locations during or just after the planetary migration phase (25, 26). The Neptune Trojans are

too faint to efficiently observe spectroscopically with current technology. The slightly red surface color observed on some outer solar system objects can be reproduced with many different compounds. Most interpretations allow about two-thirds of the reflectance gradient to be attributed to Triton tholins and one-third to ice tholins, which can be produced by bombarding simple organic ice mixtures with ionizing radiation (21, 27). However, other models have used no organic ices but simple Mg-rich pyroxene (28).

If we assume albedos for the known Trojans, we can estimate their effective radii from our photometric measurements (Table 1). The optical flux density of sunlight scattered from a solid object follows $f \propto D^2/R^4$, where D is the diameter and R is the heliocentric distance of the object. When assuming an albedo of 0.05 or 0.1 (for values in parentheses), respectively, we find the four known Neptune Trojans have radii from about 40 (30) to 70 (50) km. These sizes are comparable to the largest known Jupiter Trojans, which have albedos around 0.05.

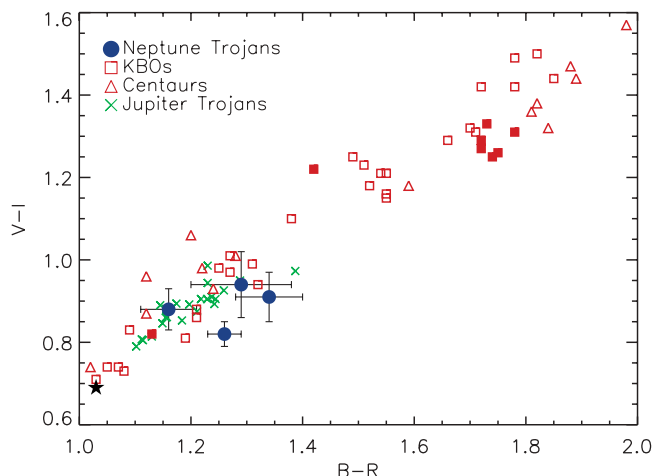
We can estimate the expected number of L4 Neptune Trojans with sizes larger than our smallest discovered object, 2005 TN₅₃, by assuming that the Trojans are equally distributed throughout the L4 Trojan cloud with identical albedos. We discovered three Trojans in about 12 square degrees. If the Neptune Trojan cloud stretched 30° in right ascension and 50° in declination near the L4 Neptune point, it would cover 1500 square degrees. Using Poisson

counting statistics, about 400^{+250}_{-200} Neptune Trojans with radii greater than about 40 (30) km are expected in the L4 Neptune cloud assuming albedos of 0.05 (0.1). The Jupiter Trojan population is complete to this size level. The Jupiter Trojan L4 cloud contains 30 (70) objects with radii greater than about 40 (30) km, whereas the L5 point harbors only about 20 (40) such objects. Depending on the albedos of the Neptune Trojans, we find they are between about 5 and 20 times more abundant at the large sizes than the Jupiter Trojans.

Through our Neptune Trojan survey and the findings discussed in (10), we find that the large Neptune Trojan size distribution may be quite steep (size distribution $q \sim 5.5$, where $n(r)dr \propto r^{-q}dr$ is the differential power-law radius distribution, with $n(r)dr$ the number of Neptune Trojans with radii in the range r to $r + dr$), which is very similar to the large Jupiter Trojans' size distribution. We found no faint Neptune Trojans (apparent red magnitude (m_R) > 24), even though our survey was sensitive to them. This may indicate a shallowing in the size distribution for the smaller Neptune Trojans, as also observed for the Jupiter Trojans (9) and KBOs (29). This may be because the largest objects have not been collisionally disrupted, whereas the smaller objects have been continually fragmented throughout the age of the Solar System.

All four known Neptune Trojans were found in the L4 region. It is likely that the Neptune L5 (trailing) region has a population of Trojans, as is true for Jupiter, but for the next several years, the line of sight through the Neptune L5 region passes near the plane of our galaxy, making observations very difficult because of stellar confusion.

Fig. 1. Optical colors of the Neptune Trojans (solid blue circles) compared with the KBOs (red squares), Centaurs (red triangles), and Jupiter Trojans (green x's). The extremely red KBOs and Centaurs are in the upper right; gray objects are in the lower left. The Neptune Trojans' colors are clearly distinct from the cold classical KBOs', which have inclinations less than 10° and KBOs with perihelions greater than 40 astronomical units (AU) (red solid squares). The Neptune Trojans are considerably more blue than the median KBO colors. The Jupiter Trojans and the blue lobe of the Centaur bimodal color distribution are similar to the Neptune Trojan colors. The color of the Sun is shown by the black star in the lower left corner. KBO and Centaur colors are from (21) and have typical error bars of 0.03 magnitudes. The Neptune Trojan color observations were obtained on photometric nights with the Magellan-Clay 6.5-m telescope with the LDSS-3 CCD camera using optical Sloan broad-band filters g' , r' , and i' . The Sloan colors were converted to the Johnson-Morgan-Cousins BVRI color system using transfer equations from (30). To verify the color transformation, we also observed an extremely red and a gray ([44594] 1999 OX3 and [19308] 1996 TO66, respectively) trans-Neptunian object. For each Trojan, we observed in all filters before repeating a filter. Each Neptune Trojan was observed on the nights of 2, 3, and 4 November 2005 universal time (UT). The standard star G158-100 was used for photometric calibration (30). Image quality was excellent with about 0.5 arc sec full width at half maximum seeing on each night. Exposure times were between 300 and 450 s for each image.



References and Notes

1. S. Peale, *Icarus* **106**, 308 (1993).
2. E. Chiang, Y. Lithwick, *Astrophys. J.* **628**, 520 (2005).
3. R. Gomes, *Astron. J.* **116**, 2590 (1998).
4. S. Kortenkamp, R. Malhotra, T. Michtchenko, *Icarus* **167**, 347 (2004).
5. F. Marzari, H. Scholl, *Icarus* **146**, 232 (2000).
6. A. Morbidelli, H. Levison, K. Tsiganis, R. Gomes, *Nature* **435**, 462 (2005).
7. F. Marzari, H. Scholl, *Icarus* **131**, 41 (1998).
8. H. Fleming, D. Hamilton, *Icarus* **148**, 479 (2000).
9. D. Jewitt, C. Trujillo, J. Luu, *Astron. J.* **120**, 1140 (2000).
10. E. Chiang *et al.*, *Astron. J.* **126**, 430 (2003).
11. J. Hahn, R. Malhotra, *Astron. J.* **130**, 2392 (2005).
12. D. Nesvorný, L. Dones, *Icarus* **160**, 271 (2002).
13. J. Horner, N. Evans, *Mon. Not. R. Astron. Soc.* **367**, L20 (2006).
14. J. Chambers, *Mon. Not. R. Astron. Soc.* **304**, 793 (1999).
15. J. Pollack *et al.*, *Icarus* **124**, 62 (1996).
16. E. Shoemaker, C. Shoemaker, R. Wolfe, in *Asteroids II*, R. Binzel, T. Gehrels, M. Matthews, Eds. (Univ. of Arizona Press, Tucson, AZ, 1989), pp. 487-523.
17. K. Tsiganis, R. Gomes, A. Morbidelli, H. Levison, *Nature* **435**, 459 (2005).
18. N. Peixinho *et al.*, *Icarus* **170**, 153 (2004).
19. S. Tegler, W. Romanishin, *Nature* **407**, 979 (2000).
20. C. Trujillo, M. Brown, *Astrophys. J.* **566**, L125 (2002).
21. M. Barucci, I. Belskaya, M. Fulchignoni, M. Birlan, *Astron. J.* **130**, 1291 (2005).

22. S. Fornasier *et al.*, *Icarus* **172**, 221 (2004).
 23. T. Grav, M. Holman, B. Gladman, K. Aksnes, *Icarus* **166**, 33 (2003).
 24. D. Jewitt, *Astron. J.* **123**, 1039 (2002).
 25. R. Gomes, *Icarus* **161**, 404 (2003).
 26. H. Levison, A. Morbidelli, *Nature* **426**, 419 (2003).
 27. A. Doressoundiram *et al.*, *Astron. J.* **125**, 2721 (2003).
 28. D. Cruikshank, C. Dalle Ore, *Earth Moon Planets* **92**, 315 (2003).
 29. G. Bernstein *et al.*, *Astron. J.* **128**, 1364 (2004).
 30. J. Smith *et al.*, *Astron. J.* **123**, 2121 (2002).
 31. We thank D. Tholen and B. Marsden for orbital discussions; J.-R. Roy, I. Jorgensen, and the Gemini observatory staff for granting and executing directors discretionary observing time; as well as D. Jewitt and

H. Hsieh for recovery observations. This paper includes data gathered with the 6.5-m Magellan telescopes located at Las Campanas Observatory, Chile, and is based in part on observations obtained at the Gemini Observatory, which is operated by the Association of Universities for Research in Astronomy, Inc., under a cooperative agreement with the NSF on behalf of the Gemini partnership: the National Science Foundation (United States), the Particle Physics and Astronomy Research Council (UK), the National Research Council (Canada), CONICYT (Chile), the Australian Research Council (Australia), CNPq (Brazil), and CONICET (Argentina). S.S.S. is supported by NASA through the Hubble Fellowship awarded by the Space Telescope Science Institute, which is operated by the Association

of Universities for Research in Astronomy, Inc., for NASA. C.A.T. is supported by the Gemini Observatory, which is operated by the Association of Universities for Research in Astronomy, Inc., on behalf of the international Gemini partnership of Argentina, Australia, Brazil, Canada, Chile, the UK, and the USA.

Supporting Online Material

www.sciencemag.org/cgi/content/full/1127173/DC1
Table S1

8 March 2006; accepted 6 June 2006

Published online 15 June 2006;

10.1126/science.1127173

Include this information when citing this paper.

Clonal Adaptive Radiation in a Constant Environment

Ram Maharjan, Shona Seeto, Lucinda Notley-McRobb, Thomas Ferenci*

The evolution of new combinations of bacterial properties contributes to biodiversity and the emergence of new diseases. We investigated the capacity for bacterial divergence with a chemostat culture of *Escherichia coli*. A clonal population radiated into more than five phenotypic clusters within 26 days, with multiple variations in global regulation, metabolic strategies, surface properties, and nutrient permeability pathways. Most isolates belonged to a single ecotype, and neither periodic selection events nor ecological competition for a single niche prevented an adaptive radiation with a single resource. The multidirectional exploration of fitness space is an underestimated ingredient to bacterial success even in unstructured environments.

Abundant bacterial variety occurs in most environments (1) and is believed to have arisen from adaptive radiation to the myriad of structured environmental and biotic niches and specialization on alternative resources (2, 3). Thus, an environment with multiple niches results in more obvious diversification of experimental bacterial populations than a homogeneous environment (4, 5). Yet the other inference from this ecological view of adaptation, that a uniform environment with a single resource leads to low sympatric diversity, has not been tested exhaustively. Understanding the rapidity and limits of bacterial diversification in defined environments would be of benefit in modeling everything from infection progression to the stability of large-scale industrial fermentations.

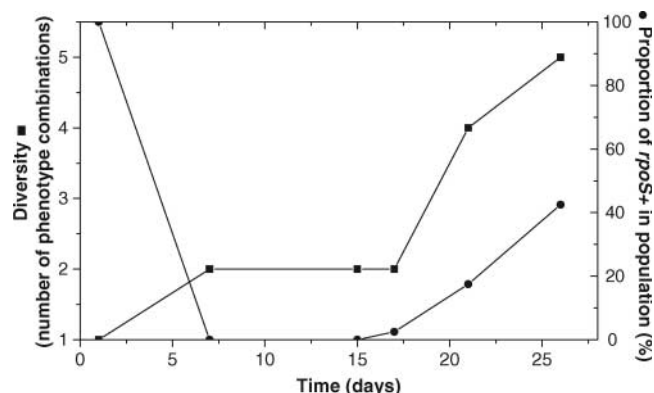
Although many mutations occur in large bacterial populations, a low phenotypic diversity is expected because of purges involving fitter mutants, called periodic selection events (6, 7). Mutational periodic selection events correlate with purifying sweeps by strongly beneficial mutations (8). Still, it is questionable whether mutational selections maintain low diversity in clonal populations (9), and several long-term experimental evolution cultures resulted in stable coexistence of clones (10, 11). The gen-

eration of new ecotypes and niches is one possible source of radiation in a restricted environment (12), with the evolution of cross-feeding polymorphisms as an example (10). The temporal and nutrient-concentration fluctuations in other intensively analyzed experimental evolution experiments (11) also cannot eliminate the possibility of specialization for unidentified niches. We explored the metabolic, phenotypic, genotypic, and ecotypic divergence in an evolving chemostat population with a constant unstructured environment and a single resource.

A screen for diversification was developed by using an *Escherichia coli* strain with a

reporter gene that can detect several types of regulatory change, resulting in improved transport properties and large fitness benefits in glucose-limited chemostats [strain BW2952 (13–15)]. As described in (16), the uniformity of populations could be tested by assaying the *malG-lacZ* fusion activity, glycogen staining, and methyl α -glucoside (α -MG) sensitivity, which detects increased glucose uptake (17). Mutations affecting *rpoS*, *mlc*, *malT*, and *ptsG* influence one or several of the assayed traits to differing extents (13). Bacteria were grown at a dilution rate (D) of 0.1 hour⁻¹ (a doubling time of 6.9 hours) with a population size of 1.6×10^{10} and sampled over 28 days. *rpoS* mutations, which confer a large fitness advantage (18), initially swept the population and led to a rapid elimination of parental *rpoS*⁺ bacteria (Fig. 1). Several identified (13) and unidentified sweeps followed the *rpoS* sweep in the dominant *rpoS* subpopulation, but the uniformity of the sampled isolates stayed high in the first 2 weeks of culture. Subsequently, and especially after 17 days, the population diversified to reveal multiple combinations of properties (Fig. 1). Simultaneously, *rpoS*⁺ bacteria again became a substantial proportion of the population. Similar diversity and recovery of *rpoS*⁺ bacteria was found in three other replicate populations (respectively, 41%, 38%, 70%, and 35% *rpoS*⁺) and prompted a more detailed analysis of late culture samples.

Fig. 1. Time course of changes in an evolving bacterial population. *E. coli* strain BW2952 was grown at $D = 0.1$ hour⁻¹ in a glucose-limited chemostat as described in (13). Daily samples were analyzed for changes in *rpoS* (circles) (16, 34). The diversity index had its basis in assays of α -MG sensitivity and *rpoS* status (both yes-no traits) and in the *malG-lacZ* activity shown in table S1



as the third trait. The fusion activity was divided into low (<200 units, wild type), intermediate (300–600 units), and high (700 units) ranges. The number of combinations of shared characters in 40 isolates tested is shown at each time point (squares).

School of Molecular and Microbial Biosciences, University of Sydney, Sydney, New South Wales 2006, Australia.

*To whom correspondence should be addressed. E-mail: tferenci@mail.usyd.edu.au